Ab initio Auxiliary-Field Quantum Monte Carlo: Formalism, Workflow, and Benchmark Applications

Amirjon Yusupov*

October 24, 2026

Abstract

The study of electronic properties and structures of strongly correlated systems presents a central challenge in condensed matter physics, where independent-electron density functional theory (DFT) struggles with static correlation and over-delocalization. The *ab initio* auxiliary-field quantum Monte Carlo (AFQMC) method provides a computational framework for solving the time-independent Schrödinger equation for various material systems, including high-T_c superconductors and transition-metal oxides. While maintaining low-order polynomial scaling, phaseless AFQMC achieves many-body wave-function-level precision, capturing intricate electron correlation effects that are typically only accessible via exponentially expensive deterministic solvers. In this study, we review the application of AFQMC to bond dissociation energies (BDEs) of diatomics and complete basis set extrapolated potential energy curves of Cr_2 and Mo_2. Furthermore, direct comparisons between AFQMC, DFT, CCSD(T), and experimental measurements are evaluated. The AFQMC method has been shown to have a maximum error reduced to 3(3) kcal/mol, with a mean absolute error (MAE) of 1.4(4) kcal/mol, thereby demonstrating close agreement with experimental observables. Ultimately, AFQMC represents one of the most advanced electronic structure methods with significant potential for providing new insights into properties of strongly correlated materials and playing a pivotal role in material discovery.

1 Introduction

The nature of strong correlations in high-T_c superconductors and transition-metal oxides has presented a profound challenge in condensed matter physics, materials science, and quantum chemistry [1]. The main difficulty lies in evaluating the quantum mechanical states of these systems; specifically, finding the exact ground state of the time-independent Schrödinger equation for the Born-Oppenheimer Hamiltonian [2]. Achieving this comes with a computational cost that scales combinatorially with the size of the studied system, limiting investigations to small molecular systems and motivating the development of approximate methods.

The most widely used approximate methods are independent-electron approaches, with density functional theory (DFT) being the standard, primary tool [3]. DFT has been extremely successful for a wide range of systems, generally scaling as the third power with system size. Its limitations, however, are equally well-documented. Among them is the inability of a standard exchange-correlation functional to accurately capture systems with degenerate or near-degenerate states [4], a defining challenge in strongly correlated materials.

Interestingly, a ranking of electronic structure methods has been created, where systematically more accurate calculations can be performed at an increasing computational cost [5, 6]. One of the most accurate quantum chemical (QC) methods is CCSD(T), which scales as the seventh power of system size [7]. There are several highly viable new approaches, including density matrix

*Independent Researcher, Samarkand, Uzbekistan. Email: amirjon.o.yusupov@gmail.com

renormalization group (DMRG) [8] and full configuration interaction quantum Monte Carlo (FCIQMC) [9]. This expands the possibilities for large-system studies at very high accuracy. In general, these methods still represent exponential computational scaling.

Auxiliary-field quantum Monte Carlo (AFQMC) is a general electronic structure method with many compelling properties [10, 11]. The AFQMC formalism integrates stochastic sampling with the DFT framework by, for instance, using Slater determinants as random walks [12]. AFQMC operates in second quantization and can incorporate other QC techniques. The defining feature of AFQMC is that it decouples two-body propagators into an ensemble of one-body propagators coupled to fluctuating auxiliary-field configurations [13]. Since AFQMC can exhibit low-order polynomial scaling with system size, with the precise scaling depending on the implementation, it delivers an excellent balance between accuracy and efficiency [10].

The remainder of this paper is organized as follows. In Section 2, we provide an overview of the DFT method and its role in computing superconducting transition temperatures; we then describe the two primary errors that drastically decrease the accuracy of DFT for transition metal systems, followed by a DFT-based comparative case study of cuprates and nickelates in Section 3. Then, in Section 4, we discuss the AFQMC method in detail, describing the key technical foundations, the emergence of the fermion sign and the phase problem, and the phaseless AFQMC (ph-AFQMC) approach that mitigates the phase problem in electronic systems [12]. Section 5 describes recent methodological advances, including frozen core, embedding, and downfolding methods; it provides a structural procedural workflow and a benchmark comparison of AFQMC performance against traditional quantum chemistry methods.

2 Localized Approximations

2.1 Density Functional Theory

Density functional theory (DFT) is a quantum mechanical method that uses electron density to model and determine the properties of matter. This effective mean-field framework uses a three-dimensional electron density as a basic variable, negating the need for a complex multi-dimensional wave function, thus mapping the solution into solvable single-electron equations in an effective background field [3, 14]. The total energy is solved for iteratively by adjusting the 3-dimensional electron density until the system converges to a minimum. This approximate functional, combined with Migdal-Eliashberg theory [15, 16], is established as a reliable method for calculating the structure and critical temperature of conventional, phonon-mediated superconductors briefly discussed in this work [17, 18].

Here, we study standard Kohn-Sham DFT, defined by an exchange-correlation functional and a single Slater determinant [3]. The former accounts for the complex quantum mechanical interactions between electrons, specifically exchange, due to the Pauli exclusion principle, and electron correlation. The Slater determinant, on the other hand, represents a non-interacting reference state that makes DFT computationally efficient and scalable, though it leaves the framework prone to errors, most notably delocalization and static correlation errors [4, 19, 20], as discussed in Section 2.2.

2.1.1 Critical Temperature

The repeated stochastic generation of structures and relaxation of the Born-Oppenheimer potential is the first step toward successful first-principles structure prediction [21]. Once the crystal structure is known, there are three other fundamental inputs needed to standardly calculate the superconducting critical temperature (T_c) [15]: (1) Kohn-Sham energies ϵ_i and wave functions $|\phi_i\rangle$; (2) phonon frequency ω_μ, representing the resonance eigenvalues of the ionic lattice; and (3) the electron-phonon matrix elements defined below:

$$g_{ij}^{\mu} = \langle \phi_i \mid \frac{\partial V_{\mathrm{KS}}}{\partial u^{\mu}} \mid \phi_j \rangle. \tag{1}$$

Afterward, these inputs have to be integrated across the Brillouin zone, which yields the Eliashberg function. In Eliashberg Theory, the phonon density of states is coupled with the electron-phonon matrix elements to construct the Eliashberg function $\alpha^2F(\omega)$, which serves as a useful tool for determining how strongly lattice vibrations glue electrons into Cooper pairs:

$$\alpha^2F(\omega) = \frac{1}{N(E_F)} \sum_{ij\mu} |g_{ij}^{\mu}|^2 \delta(\omega - \omega_{\mu}) \delta(\epsilon_i - \epsilon_F) \delta(\epsilon_j - \epsilon_F). \tag{2}$$

where $N(E_F)$ is the electronic density of states at the Fermi level. Alternatively, the semi-empirical McMillan equation can be used to predict T_c [16]:

$$T_c = \frac{\omega_{\log}}{1.2} \exp\left(-\frac{1.04(1+\lambda)}{\lambda - \mu^*(1+0.62\lambda)} \right). \tag{3}$$

where $\omega_{\log}$ is the logarithmic phonon frequency, λ is the electron-phonon coupling constant, and μ^* is the Coulomb pseudo-potential. This approach has been successful at predicting T_c for several compounds [16]. However, it has two major limitations: the McMillan equation markedly underestimates T_c for strongly coupled systems ($\lambda > 1$), an issue typically addressed via the Allen-Dynes modification; the standard harmonic approximation breaks down in hydrides due to immense quantum zero-point motion and strong anharmonic lattice effects [21]. The reader is referred to a number of research and review articles containing the details of the McMillan equation and its two major problems [22, 23].

The methods mentioned above can be used to predict the superconducting transition temperature of a specific subset of materials. In other words, DFT can be a good approximation only for certain systems. As the rest of this study will show, DFT may not be the most optimal approach for strongly correlated systems of interest, such as high-temperature superconductors and quantum materials.

2.2 DFT Errors

2.2.1 Delocalization

For fractional charges, approximate functionals increase the tendency for the charge density to spread artificially [4, 20]. Instead of the linear energy trend of the Perdew-Parr-Levy-Balduz theorem, DFT shows a convex dip in the energy graph, which is responsible for artificially lowering the energy and over-delocalizing charge. Specifically, the internal classical Coulomb interaction pushes the electron density apart. The effect compounds linearly with system size, limiting the investigation of elements and materials [4].

2.2.2 Static Correlation

Additionally, DFT does not fully capture degenerate or near-degenerate states, such as those that arise in transition metal systems, molecular bond dissociation, and strongly correlated materials, causing a severe representational limit when forcing a multi-state superposition into a single-state approximation [24, 25]. In such cases, electrons strongly entangle and form a superposition of these states. Standard DFT maps this onto non-interacting electrons, but the superposition can be very challenging to represent using a single Slater determinant. This gives rise to an unphysical energy anomaly [20].

2.2.3 High-temperature Superconductors

These theoretical errors have severe physical consequences. As demonstrated by Anisimov et al., local moments can be considerably underestimated in transition and rare-earth systems when using the local-spin-density approximation (LSDA) [26]. In cases when the calculation is performed on relatively covalent transition-metal oxides, which share the fundamental electronic features of the parent phases of cuprates and nickelates, the magnetism vanishes entirely [27]. Therefore, local approximations like LSDA can predict such systems to be non-magnetic metals, while they have been experimentally proven to be antiferromagnetic Mott or charge-transfer insulators.

The artificial quenching of magnetism is a significant limitation. The inability to reproduce the experimentally relevant magnetic state can therefore lead to an incorrect description of the low-energy electronic structure and competing phases. Hence, for unconventional superconductors, standard DFT may not be sufficient to capture the essential ground-state properties required to model the superconducting phase.

2.3 The ZSA Framework

The initial framework used to calculate band gaps was the Mott-Hubbard Theory. It was successful in describing low-energy magnetic insulators. Still, it fell short of explaining why compounds like oxides, halides, and chalcogenides of Co, Ni, and Cu have gaps tied to the electronegativity of the anion and why materials like NiS and CuS are metallic without assuming an unphysical drop in the Coulomb repulsion. It also inaccurately implies that all band gaps are *d*-*d* gaps. The unified Zaanen-Sawatzky-Allen (ZSA) theory [28] aims to resolve these limitations. Using the Anderson impurity Hamiltonian, the problem reduces to one solvable using existing many-body solutions [29, 30]. The model proves that a large *d*-*d* Coulomb interaction (U) is necessary, but not sufficient to create a large band gap. By introducing the charge-transfer energy (Δ), the model shows that band gaps can be of either a *d*-*d* character or a charge-transfer character.

U defines the energy penalty for holding two electrons in the same atomic site or the energy needed to add or remove an electron from the same atom, and Δ is the energy of the fluctuation $d_i^n \rightarrow d_i^{n+1}\underline{L}$, where $\underline{L}$ is a hole in the anion valence band. It can also be described as the energy required to move an electron from a ligand orbital, like oxygen $2p$, to a metal orbital, like copper $3d$. Δ is directly related to the Madelung potential and to the electronegativity of the anion [31, 32].

When $U < \Delta$, the band gap is proportional to U, and the material is considered to be in a 'Mott-Hubbard region'. When $U > \Delta$, the gap is proportional to Δ and is of a 'charge-transfer nature'. If $U = 0$, as assumed in some older effective one-particle potential models, the calculated E_{gap} is zero for all Δ , and the material is metallic [33].

When using the ZSA Framework, we first calculate the ground-state energy of the transition-metal impurity hybridizing with the anion valence band. The anion valence band is approximated as a semi-ellipse with a width of 3 eV, which is typical for halides [33]. The full calculation of the ground-state energy then yields the full excitation spectrum of the system, including the ligand and crystal-field splittings.

We then repeat the procedure for the states with one electron removed and obtain again the lowest-energy ionized state of the $(n-1)$-electron system (E_l^{n-1}), and the electron-affinity states, containing $n+1$ electrons, (E_A^{n+1}). This is expressed in the primary formula:

$$E_{\text{gap}}^{U<\Delta} = E_l^{n-1} + E_A^{n+1} - 2E_G^n. \tag{4}$$

For a charge-transfer insulator, the band gap is also influenced by specific hybridization shifts arising from the orbital overlap between the transition metal atom and neighboring ligands. In

the ZSA Framework, measuring these exact energy shifts is necessary to calculate the material's bandgap. Under such circumstances, the bandgap is calculated using

$$E_{\text{gap}}^{U>\Delta} = \Delta + 2\delta^{n} - \delta^{n-1} - \delta^{n+1}. \tag{5}$$

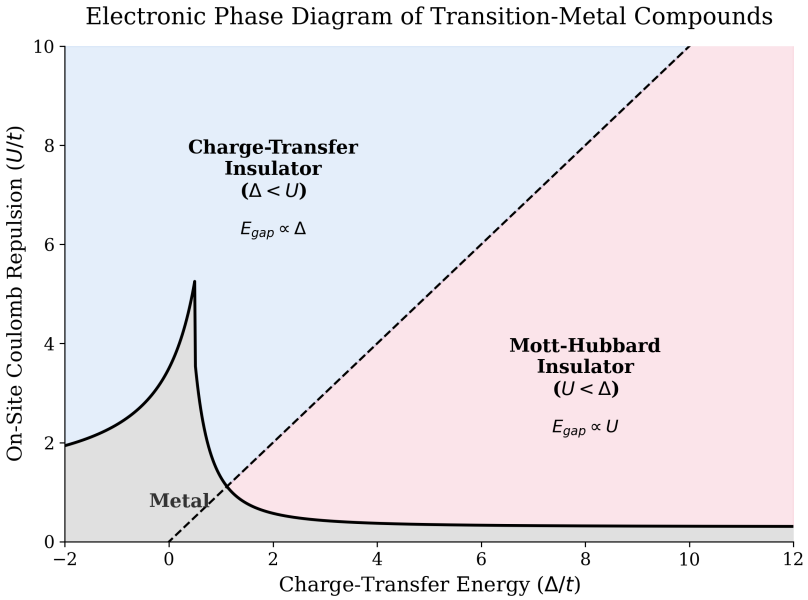

Figure 1: Schematic representation of the Zaanen-Sawatzky-Allen (ZSA) phase diagram. The diagram illustrates the competition between the on-site Coulomb repulsion (U) and the charge-transfer energy (Δ), normalized by the transfer integral (t). The dashed line $U = \Delta$ separates the Mott-Hubbard regime from the charge-transfer regime, while the solid curve denotes the metal-insulator transition boundary. Adapted from Zaanen, Sawatzky, and Allen [28].

As Figure 1 illustrates, there is an expected proportionality in both regions. Cuprates fall into the charge-transfer regime ($\Delta < U$) [1, 27], which is why their low-energy physics is explicitly a multi-orbital problem. When the kinetic hopping overcomes both U and Δ, the correlation gaps cause a metal-insulator transition (MIT) [1], shown by a metallic phase confined to the origin, where both parameters are small relative to the bandwidth.

This phase diagram demonstrates why DFT is a suboptimal approximation for narrow-band transition-metal oxides; standard Kohn-Sham DFT defines many Mott and charge-transfer systems within that metallic corner. As standard LDA and GGA functionals lack an explicit, non-local treatment of U, and struggle with the precise spatial alignment of the ligand p and metal d blocks, DFT artificially delocalizes the electrons. It forces a system that belongs in the deep insulating upper-right quadrant of the ZSA diagram down into the metallic ground state [26].

3 The Comparative Case Study

3.1 Cuprates

To demonstrate the breakdown of mean-field theory in strongly correlated systems, we compare results for $CaCuO_2$ and $LaNiO_2$.

In general, a cuprate must be doped above a critical threshold to enter a superconducting state. More unique to the copper oxides is the behaviour observed in a range of temperatures immediately above T_c in what is referred to as the pseudogap regime. The d-wave superconductivity can be invariably observed, but many competing states are close in energy, especially unidirectional

charge order. As our study focuses on the performance of electronic structure methods, the material properties will be discussed only briefly, followed by a direct demonstration of the limitations of DFT in a case study.

We identify three parameters that are particularly relevant the comparisons of transition-metal compounds.

Table 1: Electronic-structure parameters governing cuprate superconductivity.

Parameter	**Value / Ref.**	**Description**
Charge-transfer energy (Δ)	2.7 eV [34]	Inversely correlated with $T_{c,\max}$ via enhanced d-p hybridization and superexchange coupling J.
Hopping ratio ($\lvert t'/t \rvert$)	0.37 [35]	Next-nearest-neighbor kinetic hopping ratio; dictates Fermi surface curvature and stabilizes competing phase boundaries.
Crystal-field splitting (Δ_{CF})	1.5–2.5 eV [36]	Energy splitting between $d_{x^2-y^2}$ and d_{z^2} orbitals, enforcing strict single-band character at E_F.

3.2 Nickelates

$RNiO_2$ ($R = \mathrm{La}, \mathrm{Nd}$) and $CaCuO_2$ differ fundamentally in ways that strongly affect the Fermi level, band gaps, and optimal doping. In comparison, $LaNiO_2$ has a much larger charge-transfer energy $\Delta = 4.4$ eV (compared to $\Delta = 2.7$ eV in $CaCuO_2$). Because of this large gap, there is substantially less oxygen-nickel hybridization in nickelates, placing them outside the standard bounds for cuprate-like superconductivity, which was established to be in a charge-transfer regime by Zaanen *et al.* (1985).

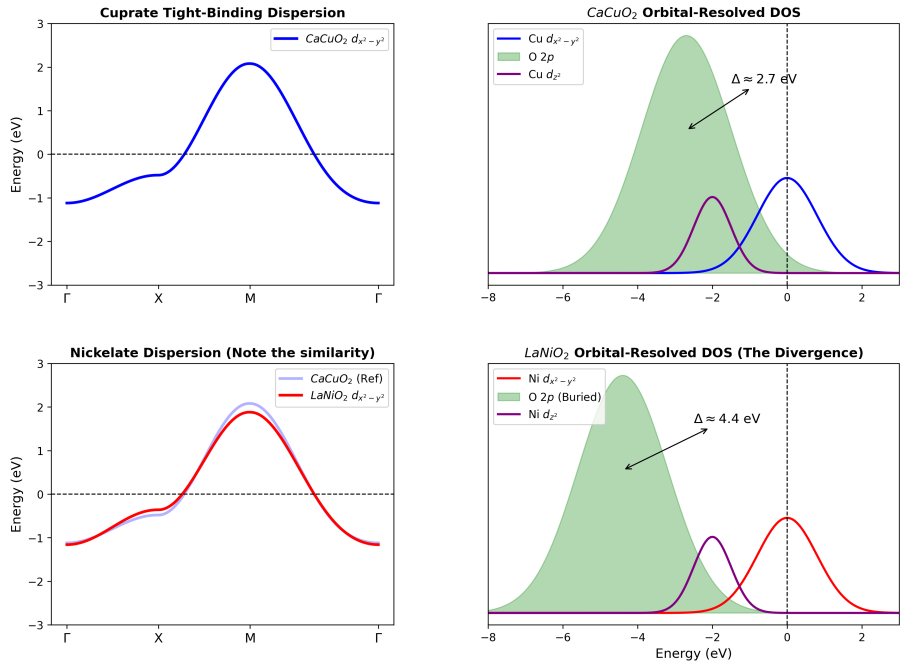

Figure 2: Comparative electronic band topology and orbital-resolved density of states (DOS) for infinite-layer $CaCuO_2$ and $LaNiO_2$. The figure highlights the conservation of longer-range hopping and orbital splitting, contrasted against an evident difference in the charge-transfer gap.

First-principles density-functional theory (DFT) calculations and tight-binding models confirm that the longer-range hopping parameter t' is highly conserved. As illustrated in the left panels of Figure 2, the $LaNiO_2$ tight-binding dispersion nearly perfectly overlaps the cuprate reference, preserving the quasi-two-dimensional Fermi surface. Similarly, the right panels show identical e_g orbital energy splitting, with the $d_{x^2-y^2}$ and d_{z^2} energy gap remaining at roughly 2 eV for both materials due to the shared absence of apical oxygens. However, there is a significant difference in the charge-transfer energy (Δ), as discussed earlier.

Beyond this widened charge-transfer gap, another striking difference is the presence of the rare-earth $5d$ states near the Fermi energy in nickelates. These rare-earth atoms are not merely passive spacer blocks; their $5d$ electrons actively participate in conduction. Because their energy overlaps the Fermi level, they create a weakly interacting, three-dimensional metallic state right between the nickel-oxygen planes, turning a clean single-band system into a multi-band one. The most critical consequence of these spacer bands dropping below the Fermi level is the creation of the self-hole-doping effect [37, 38]. This effect intrinsically dopes the nickel-oxygen planes without requiring external chemical substitution.

Crucially, while mean-field calculations like DFT + U, where an added Hubbard U term corrects the delocalization, are sufficient to extract static, single-particle parameters such as the charge-transfer energy (Δ) and longer-range hopping (t'), they have fundamental limitations when modelling the emergent many-body behaviour. For instance, mean-field simulations incorrectly predict a stable antiferromagnetic state in $LaNiO_2$, missing how dynamic fluctuations of self-doped holes destroy long-range magnetic order [39].

Since the fundamental protocol of DFT lies in mapping the solution into solvable single-electron equations in an effective background field, it often misrepresents or misses phenomena like long-range magnetic order. Furthermore, due to the use of a single Slater determinant, standard Kohn-Sham DFT does not fully describe systems with degenerate and near-degenerate states, which are characteristic of transition metals and strongly correlated systems. We therefore introduce a much more robust method: *ab initio* AFQMC. This method projects out the many-body ground state wave function and maps the many-body interactions into fluctuating external potentials using the Hubbard-Stratonovich transformation, representing the state-of-the-art numerical method for quantitative quantum chemical modelling. AFQMC has been demonstrated to be extremely accurate, favorably scalable, and parallel-efficient, enabling the study of systems where DFT may not be suitable for the problem at hand.

4 Auxiliary-Field Quantum Monte Carlo (AFQMC)

4.1 Standard Monte Carlo

We list a few key elements of the standard Monte Carlo method which will be essential to our discussions on QMC. In the most general terms, the Monte Carlo method is a statistical approach to computing integrals using random positions, called samples, whose distribution is carefully chosen. In principle, the Monte Carlo method can be used to solve any problem in statistical physics [40, 41]. There are two types of Monte Carlo sampling methods: direct sampling and Markov chain sampling.

Both approaches evaluate a probability distribution $\pi(x)$ in discrete or continuous space, and both evaluate an observable (function) $\mathcal{O}(x)$. In both cases, one evaluates:

$$\frac{1}{N}\sum_{i=1}^{N}\mathcal{O}_i \simeq \langle\mathcal{O}\rangle = \frac{\int_{-1}^{1}dx\int_{-1}^{1}dy\,\pi(x,y)\mathcal{O}(x,y)}{\int_{-1}^{1}dx\int_{-1}^{1}dy\,\pi(x,y)} \tag{6}$$

On the left side of the equation, the probability distribution $\pi(x)$ and multiple integrals

disappear. This means that the Monte Carlo method allows evaluation of higher-dimensional integrals, such as those that appear in statistical physics and other domains.

In the following, we define a, b, and c as arbitrary microstates in configuration space. Our algorithm must generate configurations a, b, and c with prescribed probabilities $\pi(a)$, $\pi(b)$, and $\pi(c)$, respectively. This means that we want to create these configurations with the help of our Monte Carlo algorithm, which is nothing but a set of transition probabilities $p(a \to b)$ for moving from one configuration to the other (from a to b).

After algebraic manipulations, we arrive at the crucial condition of detailed balance:

$$\begin{aligned} \pi(a)p(a \to b) &= \pi(b)p(b \to a), \\ \pi(a)p(a \to c) &= \pi(c)p(c \to a). \end{aligned} \tag{7}$$

The detailed balance condition is extremely important because it accurately settles the Monte Carlo simulation in the target probability distribution. The consequence of this condition, which is that the move from $a \to b$ is as likely as the move from $b \to a$ when stationary weights are equal, is that the algorithm exists in a steady state, ensuring the target distribution.

Moves between a and b proposed with an arbitrary transition probability $g(a \to b)$, respecting the detailed balance condition, are generated by the Metropolis-Hastings algorithm [42, 43], which accepts a move with probability:

$$p_{accept}(a \to b) = \min\left[1, \frac{\pi(b)g(b \to a)}{\pi(a)g(a \to b)}\right] \tag{8}$$

This is significant because the Metropolis Algorithm enables the Monte Carlo algorithm to be effective for higher dimensional integrals and perform calculations of probabilities based on ratios rather than the sum of all possible outcomes from the partition function. It enables the simulation of physical systems with hundreds of interacting particles [42].

The ergodicity of a Monte Carlo algorithm measures whether all configurations can be reached in a simulation. If that is not the case, then the algorithm is strictly nonergodic. However, if all configurations are accessible, but it takes a long time to reach them, then the algorithm is defined as practically nonergodic. To find a solution to this consequence of rare configurations, let us introduce a distinct trial probability density function $q(x)$. By multiplying and dividing by $q(x)$, the integral is reweighted:

$$I(\gamma) = \int_0^1 \frac{x^\gamma}{q(x)} q(x)dx. \tag{9}$$

These classical properties form the foundation for how the ph-AFQMC methods deploy a trial wave function to guide the walker in the phase constraint.

4.2 The Fermion Sign Problem in Monte Carlo Algorithms

As we detailed earlier, the Standard Monte Carlo is an extremely useful numerical method that uses Markov chain sampling and the Metropolis algorithm to solve problems in statistical physics [42]. However, for the random walk in Monte Carlo to work mathematically, every single probability weight $P(x)$ must be a real, non-negative number ($P(x) \geq 0$). This highlights a major limitation of the classical Monte Carlo approach: we cannot sample negative probability weights and complex numbers with a random walk.

This has significant implications for stochastic projector methods like diffusion Monte Carlo (DMC), which assume that the wave function is positive everywhere. The fermion antisymmetry implies that a many-fermion wave function cannot be positive everywhere and must take both positive and negative values. Unfortunately, probabilistic methods such as DMC can handle only positive distributions. A straightforward generalization of the diffusion Monte Carlo algorithm,

such as assigning sign variables to walkers, while formally correct, leads to the fermion sign problem and an exponentially decaying signal-to-noise ratio.

The fixed-node DMC is an alternative method for dealing with the fermion antisymmetry [44]. Although not exact, it gives ground-state energies that are usually very accurate. Furthermore, unlike other Monte Carlo methods, the fixed-node algorithm is stable in large systems. The fixed-node approximation is therefore used in almost all current large-scale applications of DMC [45]. The version described here assumes that the ground-state wave function is real and hence works only in systems with time-reversal symmetry.

While real-space methods like fixed-node diffusion Monte Carlo successfully mitigate the sign problem for continuous systems, they struggle with the multi-band orbital complexity and lattice-based interactions characteristic of strongly correlated transition-metal oxides. As we will see in subsequent subsections, auxiliary-field quantum Monte Carlo resolves this by operating in second quantization over arbitrary basis sets, providing a scalable bridge from an *ab initio* Hamiltonian to stochastic ground-state projection.

4.3 Determinant Space

In classical Monte Carlo methods, a random walker is represented as a set of three-dimensional spatial coordinates $(r_1, \ldots, r_N)$. This can lead to a nodal collapse and the sign problem, as detailed in Section 4.2. For a simulation to be antisymmetrized and avoid nodal collapse, the walker must be redefined as a state vector $|\Phi\rangle$ parameterized by an $M \times N$ matrix.

Consider a two-electron system where spin orbitals χ_i and χ_j are occupied. If the first electron occupies χ_i and the second occupies χ_j, we have:

$$\Psi_{12}^{\mathrm{HP}}(x_1, x_2) = \chi_i(x_1)\chi_j(x_2). \tag{10}$$

Conversely, if the first occupies χ_j and the second occupies χ_i:

$$\Psi_{21}^{\mathrm{HP}}(x_1, x_2) = \chi_i(x_2)\chi_j(x_1). \tag{11}$$

Each Hartree product differentiates between electrons. Nevertheless, we can attain a wave function which does not. By taking a linear combination of the two Hartree products, such a wave function would satisfy the requirement of the antisymmetry principle:

$$\Psi(x_1, x_2) = 2^{-1/2}\left(\chi_i(x_1)\chi_j(x_2) - \chi_j(x_1)\chi_i(x_2)\right), \tag{12}$$

where $2^{-1/2}$ is a normalization factor. The minus sign makes the wave function flip to negative if the two electrons are switched:

$$\Psi(x_1, x_2) = -\Psi(x_2, x_1). \tag{13}$$

From the form of (12), the wave function vanishes if two electrons occupy the same spin orbital $(i = j)$. Therefore, the antisymmetry requirement yields the typical definition of the Pauli Exclusion Principle: no more than one electron can occupy a spin orbital. The antisymmetric wave function from (12) can be expressed as a determinant

$$\Psi(x_1, x_2, \ldots, x_N) = (N!)^{-1/2} \begin{vmatrix} \chi_i(x_1) & \chi_j(x_1) & \cdots & \chi_l(x_1) \\ \chi_i(x_2) & \chi_j(x_2) & \cdots & \chi_l(x_2) \\ \vdots & \vdots & \ddots & \vdots \\ \chi_i(x_N) & \chi_j(x_N) & \cdots & \chi_l(x_N) \end{vmatrix}. \tag{14}$$

and this is a Slater determinant (SD) [46]. There is a direct correspondence between interchanging the coordinates of two electrons and interchanging two rows of a Slater determinant, which flips the sign of the determinant. Furthermore, a Slater determinant naturally coordinates the

movement of electrons with matching spins, but ignores electrons with opposite spins. The requirement of antisymmetry can also be satisfied by using second quantization. It is a formalism in which the antisymmetry property is transferred onto algebraic properties of specific operators. Second quantization shifts focus away from the complex N-electron wave function to simpler one- and two-electron integrals. If a creation operator $a_i^\dagger$ is associated with each spin orbital χ_i, then the operator relation becomes

$$a_i^\dagger a_j^\dagger + a_j^\dagger a_i^\dagger = 0 = \{a_i^\dagger, a_j^\dagger\} \tag{15}$$

where we have used the notation for the anticommutator of two operators. Since,

$$a_i^\dagger a_j^\dagger = -a_j^\dagger a_i^\dagger \tag{16}$$

we can interchange the order of operators provided we change the sign. If $i = j$, we have

$$a_i^\dagger a_i^\dagger = -a_i^\dagger a_i^\dagger = 0 \tag{17}$$

which states that we cannot create two electrons in the same spin orbital χ_i.

The same set of equations can be applied, with some changes, to an annihilation operator a_i, which annihilates or removes an electron in spin orbital χ_i. Interchanging creation and annihilation operators leads to the following operator relation

$$a_i a_i^\dagger + a_i^\dagger a_i = 1 = \{a_i, a_i^\dagger\} \tag{18}$$

As a result of the antisymmetry property of determinants, we have

$$a_i a_j^\dagger + a_j^\dagger a_i = 0 = \{a_i, a_j^\dagger\} \quad (i \neq j) \tag{19}$$

If we combine this with (18), we obtain the anticommutator relation between creation and annihilation operators:

$$a_i a_j^\dagger + a_j^\dagger a_i = \delta_{ij} = \{a_i, a_j^\dagger\} \tag{20}$$

All features of Slater determinants are completely defined by the anticommutation rules of the creation and annihilation operators. We can define a Slater determinant in the formalism of second quantization

$$a_i^\dagger a_k^\dagger \cdots a_l^\dagger |0\rangle = |\chi_i \chi_k \cdots \chi_l\rangle \tag{21}$$

Any result derived from determinants can also be proven using just the algebra of creation and annihilation operators

To completely replace determinants in many-electron theory, we must express our physical operators ($\mathcal{O}_1$ and $\mathcal{O}_2$) purely through operator algebra. We also must get the same output for matrix elements whether we use the properties of determinants or the algebra of creation and annihilation operators. The second-quantized formulas for the total one-electron operator ($\mathcal{O}_1$) and the two-electron Coulomb repulsion ($\mathcal{O}_2$) are

$$\mathcal{O}_1 = \sum_{ij} \langle i|h|j\rangle a_i^\dagger a_j \tag{22}$$

$$\mathcal{O}_2 = \frac{1}{2} \sum_{ijkl} \langle ij|kl\rangle a_i^\dagger a_j^\dagger a_l a_k \tag{23}$$

where the sum is over the set of spin orbitals $\{\chi_i\}$.

There is a key distinction between SDs in AFQMC and QC methods. In the latter, SDs are orthogonal. In AFQMC, by contrast, SDs are nonorthogonal to each other, as the occupied orbitals of each SD are continuously changed during the random walk.

The manifold of Slater determinants is closed under the action of exponentials of single-particle operators: a property fundamentally tied to the Thouless Theorem. The theorem establishes that any Slater determinant not orthogonal to a reference state can be uniquely written as such an exponential transformation. As we shall see in later sections, the significance of this closure property and the Thouless Theorem is highlighted when the AFQMC algorithm uses the Hubbard-Stratonovich Transformation to decouple electron-electron interactions into single-particle operators coupled to fluctuating auxiliary-fields.

The theorem and the underlying algebra guarantee that as long as walkers interact only with these fields, they never split into linear combinations of determinants.

Due to the Thouless Theorem, instead of propagating over an entire N-particle state vector, imaginary-time evolution reduces to updating the walkers' $M \times N$ single-particle orbital coefficient matrix via standard matrix multiplication:

$$\exp\left(\sum_{ij} h_{ij} c_i^\dagger c_j\right) |\Phi\rangle = |\Phi(e^h \Phi)\rangle \tag{24}$$

The intrinsic property of a Slater determinant is the determinantal overlap. It is the inner product that measures how much a walker's state overlaps with a chosen trial state,

$$\langle \Psi_T | \Phi \rangle = \det(\mathcal{O}) \tag{25}$$

It tracks walker statistical weights and phase changes at a lower computational cost of $\mathcal{O}(N^3)$ instead of $\mathcal{O}(N!)$.

Additionally, the Generalized Wick's Theorem is a tool used to evaluate the properties of a Slater determinant. It reconfigures multi-electron operators into combinations of Green's function entries ($G^{\Phi\Psi}_{p\sigma,q\tau}$)

$$\frac{\langle \Phi | \hat{a}^\dagger_{p\sigma} \hat{a}^\dagger_{q\tau} \hat{a}_{s\tau} \hat{a}_{r\sigma} | \Psi \rangle}{\langle \Phi | \Psi \rangle} = G^{\Phi\Psi}_{p\sigma,r\sigma} G^{\Phi\Psi}_{q\tau,s\tau} - G^{\Phi\Psi}_{p\sigma,s\tau} G^{\Phi\Psi}_{q\tau,r\sigma} \tag{26}$$

The Generalized Wick's Theorem negates the need to construct problematic two-particle matrices, allowing efficient evaluation of full two-body electron interactions.

A major benefit of second quantization is its ability to handle systems with changing numbers of particles. This makes it ideal for studying infinite systems like solids [47].

4.4 Hubbard-Stratonovich Transformation

Having defined the walker as a Slater determinant parameterized by $M \times N$ matrix in Section 4.3, we now face the problem of imaginary-time propagation. While one-body operators act on a Slater determinant as orbital rotations via the Thouless Theorem [48], the two-body Coulomb interaction $\hat{v}$ breaks the single-determinant structure.

To avoid a linear combination of exponentially many determinants, the Hubbard-Stratonovich transformation decouples two-body interactions into one-body operators coupled to fluctuating auxiliary fields [13].

The two-body part of the Hamiltonian can be written in the following form

$$\hat{H}_2 = \frac{1}{2} \sum_{\gamma=1}^{N_\gamma} \lambda_\gamma \hat{v}_\gamma^2 \tag{27}$$

where λ_γ is a constant, $\hat{v}_\gamma$ is a one-body term similar to $\mathcal{O}_1$ in (22), and N_γ is an integer. For a general two-body term, there are a number of ways to achieve the decomposition in (27). The two most commonly applied cases in electronic structure are (a) with a plane-wave basis and (b) for a denser matrix V_{ijkl} resulting from a general basis set such as Gaussians. With a general basis

in particular, the most straightforward way to decompose $\hat{H}_2$ is via direct diagonalization, which has proven to be computationally costly. Instead, we can use a modified Cholesky decomposition, which leads to $\mathcal{O}(n)$ fields [49]. This approach, which has been commonly used in AFQMC for molecular systems with Gaussian sets and for downfolded Hamiltonians [11], leads to the following equation

$$V_{ijkl} = V_{(il)(jk)} = V_{\mu\nu} = \sum_{\gamma=1}^{N_\gamma} L_\mu^\gamma L_\nu^\gamma \tag{28}$$

where $\mu = (i, l)$ and $\nu = (j, k)$ are composite indices. The process is carried out recursively using a modified Cholesky algorithm [49]. The 4-index matrix elements are represented to a predefined accuracy tolerance δ, leading to

$$\hat{H}_2 \to \frac{1}{2} \sum_{\gamma=1}^{N_\gamma} \left(\sum_{il} L_\mu^\gamma c^\dagger c_l \right) \left(\sum_{jk} L_v^\gamma c_j^\dagger c_k \right) + \mathcal{O}(\delta) \tag{29}$$

And we achieve the form in (27), where $\hat{v}_\gamma = \sum_{il} L_\mu^\gamma c_i^\dagger c_l$. We can now apply the Hubbard-Stratonovich Transformation to each term in (27)

$$e^{-\frac{\Delta\tau}{2}\lambda_\gamma \hat{v}_\gamma^2} = \int_{-\infty}^{\infty} dx \frac{e^{-\frac{1}{2}x^2}}{\sqrt{2\pi}} e^{x\sqrt{-\Delta\tau\lambda_\gamma}\hat{v}_\gamma} \tag{30}$$

where x is an auxiliary-field variable. The key concept is that we replaced the quadratic term $(\hat{v}_\gamma^2)$ on the left side of the equation with a linear one $(\hat{v}_\gamma)$ on the right. If we denote the accumulation of auxiliary fields as χ, and we combine one-body terms from $\hat{H}_1$ and $\hat{H}_2$ we get a compact representation of the outcome of the Hubbard-Stratonovich Transformation

$$e^{-\Delta\tau\hat{H}} = \int dx\, p(x)\hat{B}(x) \tag{31}$$

where $p(x)$ is a probability density function (PDF) and $\hat{B}(x)$ is a product of operators.

Importantly, the Hubbard-Stratonovich Transformation replaces the two-body interaction by one-body interactions with a set of random external auxiliary fields. In other words, it converts the interacting system into many non-interacting systems that are coupled to external fluctuating auxiliary fields. The sum over all configurations of auxiliary fields recovers the two-particle interaction.

4.5 The Phase Problem

The free-projection AFQMC suffers from an asymptotic instability in $n\Delta\tau$, which is a manifestation of the fermion sign problem in model systems [50]. For a more general interaction, such as the Coulomb repulsion, a more severe instability appears, which has been referred to as the phase problem in the literature [12]. More specifically, in free-projection AFQMC [51], the imaginary-time-dependent energy, $E(n\Delta\tau)$, is estimated by a ratio whose denominator is the expectation $\langle v \rangle_\Psi$, with $v = e^{i\theta(\Psi)}$. The expectation of the phase approaches zero exponentially with $n\Delta\tau$. This causes an increase in the variance of the MC estimate of the energy that grows exponentially. Furthermore, this rate grows with M and N, making the instability of the free-projection AFQMC more severe for large basis sets and systems. The exponential increase of statistical noise with imaginary time translates into the exponential scaling of the free-projection AFQMC.

To get a grasp of how the phase problem arises, let's recall the equation

$$|\Phi(\beta)\rangle = \int_{S(N)} d\Psi f_\beta(\Psi)|\Psi\rangle \tag{32}$$

in the overcomplete spaces of SDs. The manifold of SDs contains both the generic determinant and its negative, $-\Psi$, as distinct points. In fact, it contains $e^{i\theta}\Psi$ for any $\theta \in [0, 2\pi)$. This symmetry property has its roots in the linearity of the Schrödinger equation: if $f_\beta(\Psi)$ is a solution in (32), so is $f_\beta(e^{i\theta}\Psi) = f_\beta(\Psi)$. This can be extended to the product of operators: If $\hat{B}(x)$ in (31) is real, there are two equivalent ensembles, related by a sign change. If $\hat{B}(x)$ is complex, there are infinitely many ensembles given by different gauge choices. Thus, if $\hat{B}(x)$ is real, the sign problem arises because of the fundamental symmetry between the fermion ground-state $|\Psi\rangle$ and its negative - $|\Psi\rangle$.

Apart from special cases, the random walks will in general reach those other domains, as they are also correct representations. However, MC dynamics given by $\hat{B}(x)$ will not track "boundary" crossing into other domains, as the random walks evolve continuously. Additionally, due to the high dimensionality of $S(N)$, it will not be able to tabulate a history of where the walker has visited to estimate the sign or the phase, without incurring exponential scaling. This results in an exponentially fast decay in the signal-to-noise ratio.

In the framework of a numerical simulation, one can achieve control of the sign by breaking symmetry in the imaginary-time evolution or preventing walkers from crossing into other domains.

For real $\hat{B}(x)$, breaking symmetry can be achieved by deleting walkers whose overlap with the trial wave function $|\Psi_T\rangle$ changes sign, that is, when Ψ crosses the hypersurface $\omega\Psi = \langle\Psi_T|\Psi\rangle = 0$. The resulting approximation forms the basis of the constrained-path AFQMC, which demonstrated very accurate results for lattice models of correlated electrons [52].

In summary, the phase problem arises because a walker's overlap with a trial ground-state wave function becomes zero. As imaginary time progresses ($\tau \to \infty$), the population of walkers drifts across the zero boundary. The walkers become symmetric between their positive and negative counterparts. When a free-projection AFQMC is used to evaluate an observable, the positive and negative contributions asymptotically cancel each other out, leaving a signal-to-noise ratio decaying exponentially to zero.

4.6 Importance Sampling

As we discussed in Section 4.5, for real-valued propagators, the problem can be described as a sign problem: the random walk can cross from one sign domain to another. For complex propagators, the overlap is complex, so the problem can be described as a phase problem: the overlap can rotate continuously in the complex plane.

To control the sign problem, we introduce the importance-sampling transformation. It has been widely used as a variance-reduction measure for systems with real propagators [52, 53]. However, in complex systems, it can be used not only as a variance-reduction measure, but also to define a gauge condition.

Due to the shift freedom, we can use the Hubbard-Stratonovich representation to rewrite a shift auxiliary field (x)

$$E(n\Delta\tau) \simeq \frac{\int \prod_{l=0}^{n-1} dx_l \, p(x_l - \bar{x}_l)\langle\Psi_T|\hat{H}|\Psi_n\rangle}{\int \prod_{l=0}^{n-1} dx_l \, p(x_l - \bar{x}_l)\langle\Psi_T|\Psi_n\rangle} \tag{33}$$

We can then apply the similarity transformation along each step of the random walk path using

the overlap ratio to obtain an equivalent form

$$E(n\Delta\tau) \simeq \frac{\int \prod_{l=0}^{n-1} dx_l \, p(x_l) I(x_l, \bar{x}_l; \Psi_l) \frac{\langle \Psi_T | \hat{H} | \Psi_n \rangle}{\langle \Psi_T | \Psi_n \rangle}}{\int \prod_{l=0}^{n-1} dx_l \, p(x_l) I(x_l, \bar{x}_l; \Psi_l)} \tag{34}$$

where the importance function is defined as follows

$$I(x_{l'}, \overline{x}_{l'}; \Psi_l) = \frac{\langle \Psi_T | \hat{B}(x - \overline{x}) | \Psi \rangle}{\langle \Psi_T | \Psi \rangle} \exp\left(x \cdot x_l - \frac{\overline{x}^* \overline{x}}{2} \right) \tag{35}$$

The first factor measures how the proposed propagation changes the trial-state overlap, and the second factor corrects for the shifted Gaussian sampling distribution.

After introducing the local mixed estimator $\frac{\langle \Psi_T | \widehat{A} | \Psi \rangle}{\langle \Psi_T | \Psi \rangle} \equiv \langle \widehat{A} \rangle_m$ and expanding $logI(x_l, \overline{x}_l; \Psi_l)$ in a Taylor series, it is evident that

$$\overline{x}_\gamma = -\sqrt{\Delta\tau} \langle \widehat{v}_\gamma \rangle_m \tag{36}$$

cancels large fluctuations in the importance function, leading to a more stable random walk. The dynamic shift, which is referred to in the literature as the force bias [54], modifies the MC sampling of the auxiliary fields by shifting the center of the Gaussian according to the overlap function $\langle \Psi_T | \Psi \rangle$.

By the use of a force bias, the importance-sampling transformation can guide the walker away from $S(N)$ where $\omega(\Psi) \simeq 0$ as $\overline{x}$ diverges. When the propagators are real, the transformation imposes an infinite barrier at $\omega(\Psi) \simeq 0$, preventing walkers from crossing into other sign domains. Ultimately, this removes the sign problem. However, the importance-sampling transformation and force bias on their own cannot remove the phase problem.

With complex Hubbard-Stratonovich operators, the random walk has a rotational phase symmetry. As the propagation time grows, the overlap can undergo a rotationally invariant random walk, and walkers can accumulate near the origin. While importance sampling stabilizes local fluctuations, it cannot stop this long-time phase diffusion. Therefore, to achieve complete control of the phase problem, we need to combine the importance sampling with the phaseless approximation described next.

4.7 Phaseless Approximation

From the expressions of the importance function and local energy, the role of $\omega(\Psi) = 0$ becomes evident and easy to notice: both quantities involve fractions with denominator $\omega(\Psi)$, which diverges at the origin of the complex plane, causing large fluctuations in AFQMC calculations. Attempts to solve this problem with a force bias from (36) showed poor results [12], indicating the need to use a modified, complex force bias instead.

In the framework of electronic structure AFQMC simulations, control of the phase problem is achieved by the real local energy and phaseless approximations. The real local energy approximation replaces the $E_{loc}(\Psi)$ term in the importance function by its real part, leading to positive and real weights. The bias of this approximation becomes smaller as the trial wave function approaches the exact ground state. The phaseless approximation aims to break the rotational invariance of random walks undergone by the overlap $\omega(\Psi)$ by projecting them onto straight lines that evolve adaptively. The projection is accomplished by redefining the importance function

$$I(x, \overline{x}; \Psi) \simeq e^{-\Delta\tau(\mathrm{Re}E_{loc}(\Psi) - E_0)} \times \max(0, \cos(\Delta\theta)) \tag{37}$$

where the exponential calculates the real magnitude of the weight, and the 'cos' factor measures how much each step changes the overlap phase. Notice that, when the operators $\hat{v}_\gamma$ are real-valued, $\Delta\theta = 0$ or π, so $\max(0, \cos(\Delta\theta)) = 1, 0$, respectively, the phase projection reduces to the constrained-path AFQMC.

The resulting method is the state-of-the-art electronic structure ph-AFQMC method for real materials [10, 12]. The ph-AFQMC differs from fp-AFQMC in that it updates walkers and weights

$$\begin{aligned} |\Psi_{k+1,w}\rangle &= \hat{B}(x_{k,w} - \overline{x}_{k,w})|\Psi_{k,w}\rangle \\ W_{k+1,w} &= I(x_{k,w'}, \overline{x}_{k,w'}; \Psi_{k,w})W_{k,w} \end{aligned} \tag{38}$$

where the force bias and importance function are given by (36) and (37), and $\theta_{k,w} \equiv 0$.

5 *Ab initio* AFQMC workflow

5.1 Generating the *ab initio* Hamiltonian

The fundamental step in the *ab initio* AFQMC method is to retain the many-electron Hamiltonian while sampling the ground-state projection stochastically.

The many-electron Schrödinger equation in the Born-Oppenheimer approximation is defined as

$$\hat{H} = H_0 + \hat{H}_1 + \hat{H}_2 = H_0 + \sum_{\substack{pq \\ \sigma}} h_{pq}\hat{a}^\dagger_{p\sigma}\hat{a}_{q\sigma} + \frac{1}{2}\sum_{\substack{pqrs \\ \sigma\tau}} v_{pqrs}\hat{a}^\dagger_{p\sigma}\hat{a}^\dagger_{q\tau}\hat{a}_{s\tau}\hat{a}_{r\sigma} \tag{39}$$

where H_0 is internuclear repulsion and $\hat{a}^\dagger_{p\sigma}\hat{a}_{q\sigma}$ are annihilation and creation operators.

The matrix elements of one- and two-electron integrals are

$$h_{pq} = \int dr\, \Phi^*_p(r)\left(-\frac{1}{2}\frac{\partial^2}{\partial r^2} - \sum_{a=1}^{N_n}\frac{Z_a}{|r - R_a|}\right)\Phi_q(r) \tag{40}$$

$$v_{pqrs} = \int dr \int dr'\, \Phi^*_p(r)\Phi^*_q(r')\frac{1}{|r - r'|}\Phi_r(r)\Phi_s(r') \tag{41}$$

where h_{pq} is a one-electron integral that contains kinetic energy and electron-nucleus interaction, and v_{pqrs} is a two-electron integral that contains many-body Coulomb interaction. Once we represent electron interaction as a 4-index tensor v_{pqrs}, the Hamiltonian is mathematically explicit and suitable for AFQMC. However, storing and manipulating that tensor has been proven to be computationally costly [55], which is why we introduce the Cholesky decomposition as a solution in Section 5.2.

The typical molecular AFQMC uses molecular orbitals (MO) obtained by orthogonalizing atom-centered Gaussian basis functions. The underlying atomic orbital (AO) integrals can be produced by standard quantum-chemistry software, then transformed into the MO basis used by AFQMC. This highlights a crucial connection between mean-field and stochastic methods in our framework: DFT is a practical independent-electron calculation that supplies orbitals and trial determinants; AFQMC applies the ground-state projection using the resulting Hamiltonian representation.

In AFQMC, the use of a finite basis inevitably introduces an approximation. Since the number of predefined basis functions is finite, the set cannot span the full, multi-dimensional Hilbert space. However, this can be removed by extrapolating results to the complete basis set (CBS) limit, which is typical of Quantum chemical (QC) methods [10].

5.2 Cholesky Decomposition

The two-electron integral v_{pqrs} has four orbital indices. In a basis of size M, the tensor has $\mathcal{O}(M^4)$ entries. However, it would be highly impractical for the AFQMC algorithm to recursively sample

an unrestricted four-index integral. Representing v_{pqrs} as a sum $v_{pqrs} = \sum_\gamma L^\gamma_{pr} L^\gamma_{qs}$ in which indices pr and qs are uncoupled, leads to the form from (27) needed for the Hubbard-Stratonovich transformation [56]

$$\hat{v}_\gamma = i \sum_{pq} L^\gamma_{pq} \sum_\sigma \hat{a}^\dagger_{p\sigma} \hat{a}_{q\sigma} \tag{42}$$

When real-valued orbitals are used as a one-electron basis set, the interaction tensor can be reshaped into a symmetric and positive definite matrix $V_{\mu(pr)\nu(qs)} = v_{pqrs}$, which can then be approximated using a modified Cholesky decomposition (mCD) [49, 57]. The mCD recursively adds the largest residual diagonal contribution until the representation error falls below the chosen threshold δ. Given $N_\gamma \geq 0$ Cholesky vectors $V_{\mu\nu}$, which also represent the number of auxiliary fields in the HS transformation, can be expressed as

$$V_{\mu\nu} = \sum_{\gamma=1}^{N_\gamma} L^\gamma_\mu L^\gamma_\nu + \Delta^{(N_\gamma)}_{\mu\nu} \tag{43}$$

where $\Delta^{(N_\gamma)}_{\mu\nu}$ is a residual error matrix at the N_γ-th iteration.

The typical values of δ range between 10^{-6} and 10^{-4}. Executing the modified Cholesky decomposition of $V_{\mu\nu}$ takes $\mathcal{O}(M^3)$ operations and memory, and leads to $\mathcal{O}(M)$ vectors. By contrast, direct diagonalization of $V_{\mu\nu}$, which was commonly used in earlier AFQMC methods, results in $\mathcal{O}(M^2)$ vectors and takes $\mathcal{O}(M^6)$ operations and $\mathcal{O}(M^4)$ storage, which is very inefficient for large systems.

5.3 Frozen core, embedding, and downfolding

Due to the general form of the Hamiltonian from (39), the treatment of core electrons is relatively straightforward. Furthermore, an effective core potential (ECP) can be implemented in the same manner as for other QC methods, using a modified Hamiltonian and appropriate basis sets [58].

The implementation of a frozen core approximation in AFQMC is also relatively simple [59]. We proceed by introducing the separability approximation for a partition of the many-body ground state into "active" and "inactive" spaces

$$|\Psi_{gs}\rangle = \left(\prod_{i=1}^{N_I} \hat{a}^\dagger_{\phi i\uparrow} \hat{a}^\dagger_{\phi i\downarrow} \right) |\Psi_A\rangle \tag{44}$$

where Ψ_A is a wave function representing spin-σ electrons in the Fock space spanning the active orbitals. Crucially, the first N_I electrons of a spin occupy inactive orbitals, which are typically defined at a low level of DFT or HF theory. These inactive orbitals are constrained to remain doubly occupied and frozen. Active and inactive orbitals span different sectors of a one-electron Hilbert space. Therefore, to construct a ground state wave function within the frozen core approximation, we only need to simulate an effective active space Hamiltonian

$$\widehat{H}_A = H'_{A,0} + \widehat{H}'_{A,1} + \widehat{H}'_{A,2} \tag{45}$$

where the two-body term $\widehat{H}'_{A,2}$ is the interaction projected into the active space. The scalar and one-body terms $H'_{A,0}$, $\widehat{H}'_{A,1}$ are modified such that the frozen core still contributes to the energy and core-valence interactions.

Quantum embedding is a different application of this same method. The main idea is to embed a local region of the system in an environment frozen at the independent-electron level. A prominent application of this technique is the study of adatom adsorption on cobalt-intercalated graphene [60].

Another application that proved highly effective is called downfolding. DFT calculations that involve large plane-wave bases are performed, yielding a set of M_{pv} orbitals. The key idea of this application is to retain the first M low-energy orbitals as a basis set for AFQMC, while discarding high-order orbital effects. This approach has been commonly used in combination with the frozen core approximation in which core orbitals are frozen at the DFT level. Downfolding led to more accurate calculations compared to conventional pseudopotentials when both techniques were applied to systems under high pressure [61].

We can focus on low-energy states in the Hilbert space to reduce the degrees of freedom. The entire workflow can be summarized succinctly: The independent-electron calculation, such as unrestricted DFT, is performed, yielding a set of M orbitals. Some of the lowest-energy orbitals are frozen, and some of the high-energy virtual orbitals are discarded, creating an active space. We then obtain an effective Hamiltonian for the active space and use it to perform a standard AFQMC calculation.

5.4 The guiding trial wave function

The trial wave function Ψ_T is highly important in AFQMC. It is the key part of the importance sampling and the phase constraint. The closer Ψ_T is to the exact ground state, the smaller the local energy fluctuations. In constrained calculations, Ψ_T can also establish the accuracy of the phase constraint and the efficiency of the importance sampling, indicating its significance within these two techniques and the AFQMC algorithm as a whole.

When the mixed estimator is used with the constrained-path or phaseless approximation, it can give a nonvariational estimate of the ground state energy [12]. Higher-quality trial wave functions Ψ_T can mitigate this nonvariationality. Furthermore, the choice of a single Slater determinant as a trial wave function demonstrated excellent accuracy [11].

However, when several electronic configurations are near-degenerate, which usually happens in dissociation bonds or in transition metals, as we will see in Section 5.6, the multideterminant trial wave function is commonly used

$$|\Psi_T\rangle = \sum_{d=1}^{N_d} A_d |\Psi_d\rangle \tag{46}$$

It improves the accuracy, reduces step-size errors, local energy fluctuations, and the imaginary time it takes for the walker ensemble to equilibrate [62].

The same theories that we used for a single Slater determinant, namely the determinantal overlap, one-particle Green's function, Thouless theorem, and the generalized Wick's theorem, can be straightforwardly generalized to multideterminant trial wave functions by treating each configuration Ψ_d separately in the linear combination [48, 63]. We can compute the overlap and Green's function using the following equations:

$$\langle \Psi_T | \Psi \rangle = \sum_{d=1}^{N_d} A_d^* \langle \Psi_d | \Psi \rangle \tag{47}$$

$$G_{p\sigma,q\tau}^{\Psi_T \Psi} = \frac{\sum_{d=1}^{N_d} A_d^* \langle \Psi_d | \Psi \rangle G_{p\sigma,q\tau}^{\Psi_d \Psi}}{\sum_{d=1}^{N_d} A_d^* \langle \Psi_d | \Psi \rangle} \tag{48}$$

5.5 AFQMC Algorithm

The overall numerical algorithm for the imaginary time propagation follows a ten-step framework established by Motta and Zhang [10]. It outlines the core parts of the algorithm that contribute to the overall efficiency and accuracy of the *ab initio* AFQMC method. As it is evident from the ten-step framework below, every major theory, approximation technique, and function introduced throughout Sections 4 and 5 plays an important role in a simulation:

1. Initialize each walker state, setting statistical weight $W = 1$ and the phase factor to zero.
2. For non-zero statistical walker weights, compute the overlap $\langle \Psi_T | \Psi \rangle$ and the force bias.
3. Sample an auxiliary field vector $\mathbf{x}$ to advance the walker by an imaginary time-step $\Delta\tau$.
4. Evaluate the updated walker's overlap with the trial wave function Ψ_T.
5. Update the weight and phase of the walker.
6. In a constrained-path calculation, discard the phase factor while applying the cos projection.
7. To create one step of the random walk, repeat steps 2-6 for all walkers.
8. Apply population control at regular time intervals to branch or destroy walkers based on their accumulated weights.
9. Reorthonormalize the orbital coefficient matrices of each walker periodically to maintain numerical stability.
10. Repeat this process until sufficient measurements have been accumulated.

5.6 Benchmark Applications

Having detailed the important parts of the *ab initio* AFQMC formalism, we now analyze representative published benchmarks for various observables, including bond breaking, bond dissociation energies of diatomics, and complete basis set extrapolated potential energy curves of transition-metal dimers. We also compare the performance of the AFQMC method to standard DFT and single-reference coupled cluster methods in strongly correlated regimes of interest [7].

5.6.1 Bond breaking

The AFQMC method has been used to study bond stretching and breaking in various chemical systems. In the compression regime, where internuclear distances are small, dynamical interactions form the ground state, and they can be accurately captured by single-reference methods such as coupled cluster; in the dissociation regime, where internuclear distances are large, there may be more than one important electronic configuration due to quasi-degeneracies, in which case a single Slater determinant cannot accurately describe the system.

The AFQMC method has been applied to several chemical systems. In most such cases, the ph-AFQMC method exhibits better overall accuracy and delivers a more balanced description than CCSD(T).

The hydrogen-chain benchmark tests whether the AFQMC method retains its accuracy across the entire potential energy curve and into the complete basis set and thermodynamic limits. As shown in Figure 3, AFQMC is in excellent agreement with high-level reference calculations [64].

5.6.2 Symmetries

Symmetry properties play an important role in the efficiency and accuracy of AFQMC. Typically, systems have symmetries, meaning operators commute with the Hamiltonian $\hat{H}$. In the ideal case, approximate eigenfunctions of $\hat{H}$ are eigenstates of the Hamiltonian symmetries with appropriate eigenvalues.

One of the most important symmetries is that of total spin, in which the total spin-squared, $\hat{s}^2$, commutes with $\hat{H}$. The total spin-squared can have different eigenfunctions, including Restricted open-shell Hartree-Fock (ROHF) with eigenvalue $\lambda = \frac{N_\uparrow - N_\downarrow}{2}\left(\frac{N_\uparrow - N_\downarrow}{2} + 1\right)$. An unrestricted Hartree-Fock (UHF) determinant, however, generally is not an eigenfunction due to

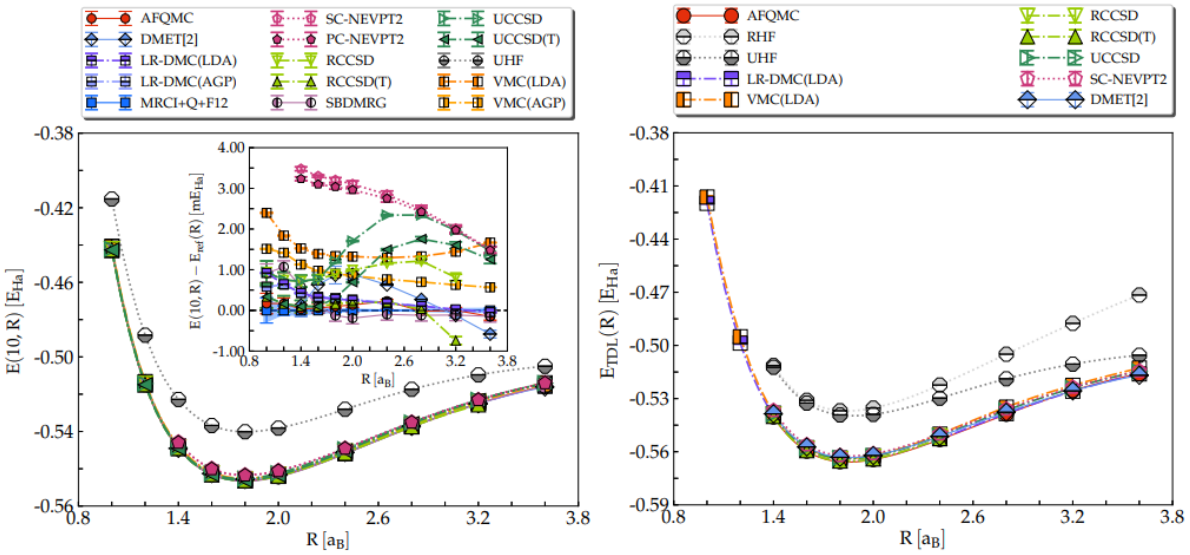

Figure 3: Left: Energy per atom of H_{10} in the complete basis set (CBS) limit against the distance R between two consecutive H atoms. Right: potential energy curve per atom of the H chain. Reprinted with permission from M. Motta and S. Zhang, WIREs Comput. Mol. Sci. 8, e1364 (2018) [10]. Copyright 2018 Wiley Periodicals, Inc.

spin contamination. If a certain approximate wave function is an eigenfunction of $\hat{s}^2$, then it is called spin pure. However, if it is not an eigenfunction, it is called contaminated.

The AFQMC projection restores spin symmetry stochastically, leading to a spin-pure ground state. If the trial wave function Ψ_T is part of the phaseless constraint, spin-contaminated components can survive, causing systematic errors in the calculation. One way to solve this is by choosing a population of random walkers with spin-pure Slater determinants. We can achieve this by using an ROHF-type wave function as an unrestricted initial wave function $|\Psi_I\rangle$ to initialize the population. Since each random walk along the imaginary-time propagation is spin-pure, spin-contaminated components can be straightforwardly projected out [65].

At the HF level, broken spatial symmetries can occur in open-shell systems. These symmetries can be restored by performing an active space expansion in the subsystem of the open-shell or using the symmetry restoration technique.

5.6.3 Comparisons of ph-AFQMC with DFT and CC methods

As we have detailed in Sections 2 and 3 of our study, DFT suffers from delocalization and static correlation errors when applied to strongly correlated systems, such as transition metal oxides. However, it is important to define how much DFT calculations and their results differ from those by ph-AFQMC and Coupled-cluster (CC) methods. This would eventually help to determine the most optimal computational method for the problem at hand. We therefore draw upon the comprehensive benchmark study by Shee et al. [66], analyzing the bond dissociation energies (BDEs) of 41 transition metal-containing diatomics across 10 DFT functionals, CC methods, and ph-AFQMC compared directly against experimental measurements.

In their dataset, Shee et al. established a baseline set of experimental measurements primarily from de Oliveira-Filho et al., supplemented by high-quality results from Dixon et al. [67, 68]. Cases exhibiting unresolved experimental disagreement within error bars were excluded, leaving CrO as the sole omitted system.

Since dynamic correlations are not included in the treatment of spin-orbit effects at the complete active space self-consistent field (CASSCF) level, DeYonkers et al. suggested that the "chemical accuracy" for transition-metal systems be within 3 kcal/mol [69]. None of the DFT

functionals in this study meet this criterion.

Table 2: Mean Absolute Error and Maximum Error on D_e for ph-AFQMC, CCSD(T), and DFT methods against the experiments. The test set includes 41 diatomics.

Method	MAE	Max Error
PBE	15.66	40.90
BP86	14.78	38.17
TPSS	12.83	31.00
M06-2X	12.05	37.95
BLYP	11.64	37.10
M06-L	8.44	21.85
M06	7.06	22.25
PBE0	4.73	21.85
B3LYP	4.45	23.45
B97	3.70	17.25
CCSD(T)	2.84	17.35
icMRCCSD(T)	2.76	11.60
QMC/MP2cbs	2.3(4)	12(2)
QMC/CCcbs	2.1(4)	7(2)
QMC/MP2+QZcbs†	1.5(4)	4(3)
QMC/CC+QZcbs†	1.4(4)	3(3)

† Includes QMC TZ/QZ CBS extrapolations when available

As is well known, the accuracy of the DFT method relies entirely on the functional deployed. That is the reason why mean absolute errors (MAEs) for 10 DFT functionals from Table 2 vary from 15.66 to 3.70 kcal/mol. As the study suggests, the most accurate functional is B97, with an MAE of 3.70 kcal/mol and a maximum error of 17.25 kcal/mol; thus, it is recommended that it is deployed in DFT studies of transition-metal systems. However, due to its lower MAE, CCSD(T) is preferred over DFT in a head-to-head comparison, assuming one has adequate computing capacity.

For CCSD(T) and icMRCCSD(T), the study shows MAEs of 2.84 and 2.76 kcal/mol, and maximum errors of 17.35 and 11.60 kcal/mol, respectively. Although CC methods are considered the "gold standard" of quantum chemistry, Shee et al. believe that a robust benchmark method cannot make such large errors for individual cases. However, they note that a number of assumptions could have caused such suboptimal accuracy, with additivity assumptions being the primary cause. In principle, CC methods can be made more accurate when a rigorous computational protocol is utilized, with the assumption that one is willing to bear the higher computational expense required to carry out such a protocol.

When it comes to the ph-AFQMC method, QMC/MP2cbs demonstrated an MAE of 2.3(4) kcal/mol and a maximum error of 12(2) kcal/mol. This is arguably slightly more robust than CCSD(T), which scales as the seventh power with system size. It is truly remarkable because CCSD(T) involves CC calculations, while QMC/MP2cbs requires the ph-AFQMC calculation in a triple-zeta (TZ) basis set only. The two major advantages of the QMC approach are its near-perfect parallel efficiency and its adaptability for GPU acceleration. The lowest MAE reported in this benchmark was obtained by QMC/CC+QZcbs, with a maximum error reduced to 3(3) kcal/mol and an MAE of 1.4(4) kcal/mol.

5.6.4 Transition-metal dimers

Transition metals present an outstanding challenge for numerical methods due to the presence of strong static and dynamic electronic correlations in them. The complexity of bonding in

these systems resembles the balance between competing tendencies commonly found in strongly correlated materials. Group VIB dimers are particularly interesting because their properties result in a many-body energy spectrum with many strong electronic correlation effects and nearly degenerate states.

AFQMC has been successfully applied to examine potential energy curves of two such dimers, chromium dimer Cr_2 [70] and molybdenum dimer Mo_2 [71]. For Mo_2, the most advanced QC methods have given widely different results. As for Cr_2, it is known as a major benchmark challenge in quantum chemistry, featuring a formal sextuple bond, a short equilibrium bond length (~ 1.7 Å), and weak binding energy (1.5 eV).

For each case, AFQMC has given one of the most accurate theoretical results of the potential energy curve, which is evident from Figure 4. The presence of strong static correlation in both molecules required the use of a multideterminant trial wave function. The results are extrapolated to the complete basis set (CBS) limit with standard methods.

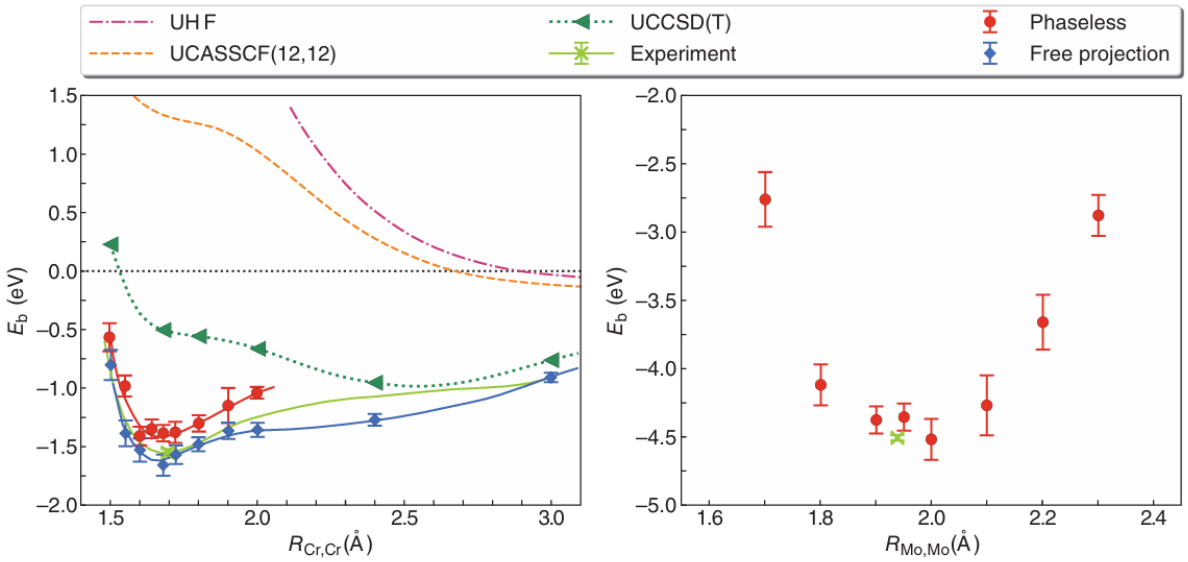

Figure 4: Left: complete basis set (CBS) extrapolated potential energy curve of Cr_2 from ph-AFQMC and free projection AFQMC compared to experiment, UHF, UCCSD(T), UCASSCF(12, 12). Right: CBS-extrapolated potential energy curve of Mo_2 compared to experiment. Reproduced with permission from M. Motta & S. Zhang (2018) [10]. Copyright 2018 John Wiley & Sons, Inc.

6 Conclusion

In spite of the fundamental complexity of solving the many-electron Schrödinger equation, increasingly more accurate electronic structure methods have been developed. Driven by the rapid expansion of computing resources, many-body computational methods will be central to providing new insights into material properties. Therefore, in conjunction with experiment, this will very likely lead to the discovery of numerous new materials, including high-T_c superconductors and quantum materials, and a much more robust understanding of the quantum mechanical behaviour of such interacting systems.

In this study, we have provided a comprehensive overview of the AFQMC method and demonstrated its excellent accuracy by analyzing bond dissociation energies and MAEs in 41 diatomics, based largely on the study by James Shee et al. [66]. A detailed comparison of CBS-extrapolated potential energy curves of Cr_2 and Mo_2 between the AFQMC method, UHF,

and CCSD(T) is also provided, showing a remarkable agreement between AFQMC calculations and experimental measurements [70, 71].

Since the accuracy of the AFQMC method is highly dependent on the quality of trial wave functions, much effort is put into reducing this systematic bias by extracting better trial wave functions from CASSCF [65, 72] and novel machine learning methods, such as Neural Network Quantum States (NNQS) [73]. Furthermore, extensions of the AFQMC method to finite temperatures are much desirable, as they would enable first-principles mapping of quantum phase transitions and electronic phase diagrams [74].

References

[1] M. Imada, A. Fujimori, and Y. Tokura. Metal-insulator transitions. *Reviews of Modern Physics*, 70(4):1039–1263, 1998.

[2] M. Born and R. Oppenheimer. Zur Quantentheorie der Molekeln. *Annalen der Physik*, 389 (20):457–484, 1927.

[3] W. Kohn and L. J. Sham. Self-consistent equations including exchange and correlation effects. *Physical Review*, 140(4A):A1133–A1138, 1965.

[4] P. Mori-Sánchez, A. J. Cohen, and W. Yang. Localization and delocalization errors in density functional theory and implications for band-gap prediction. *Physical Review Letters*, 100(14):146401, 2008.

[5] T. Helgaker, W. Klopper, H. Koch, and J. Noga. Basis-set convergence of correlated calculations on water. *The Journal of Chemical Physics*, 106(23):9639–9646, 1997.

[6] J. P. Perdew and K. Schmidt. Jacob's ladder of density functional approximations for the exchange-correlation energy. In *AIP Conference Proceedings*, volume 577, pages 1–20, 2001.

[7] K. Raghavachari, G. W. Trucks, J. A. Pople, and M. Head-Gordon. A fifth-order perturbation comparison of electron correlation theories. *Chemical Physics Letters*, 157(6):479–483, 1989.

[8] S. R. White. Density matrix formulation for quantum renormalization groups. *Physical Review Letters*, 69(19):2863–2866, 1992.

[9] G. H. Booth, A. J. W. Thom, and A. Alavi. Fermion Monte Carlo without fixed nodes: A game of life, death, and annihilation in slater determinant space. *The Journal of Chemical Physics*, 131(5):054106, 2009.

[10] M. Motta and S. Zhang. Ab initio computations of molecular systems by the auxiliary-field quantum Monte Carlo method. *WIREs Computational Molecular Science*, 8(5):e1364, 2018.

[11] W. A. Al-Saidi, S. Zhang, and H. Krakauer. Auxiliary-field quantum Monte Carlo calculations of molecular systems with a Gaussian basis. *The Journal of Chemical Physics*, 124 (22):224101, 2006.

[12] S. Zhang and H. Krakauer. Quantum Monte Carlo method using phase-free random walks with Slater determinants. *Physical Review Letters*, 90(13):136401, 2003.

[13] R. L. Stratonovich. On a method of calculating quantum distribution functions. *Soviet Physics-Doklady*, 2:416–419, 1957.

[14] R. G. Parr and W. Yang. *Density-Functional Theory of Atoms and Molecules*. Oxford University Press, New York, 1989.

[15] F. Giustino. Electron-phonon interactions from first principles. *Reviews of Modern Physics*, 89(1):015003, 2017.

[16] P. B. Allen and R. C. Dynes. Transition temperature of strong-coupling superconductors. *Physical Review B*, 12(3):905–922, 1975.

[17] A. D. Becke. Density-functional thermochemistry. III. The role of exact exchange. *The Journal of Chemical Physics*, 98(7):5648–5652, 1993.

[18] J. P. Perdew, K. Burke, and M. Ernzerhof. Generalized gradient approximation made simple. *Physical Review Letters*, 77(18):3865–3868, 1996.

[19] A. J. Cohen, P. Mori-Sánchez, and W. Yang. Fractional spins and static correlation error in density functional theory. *The Journal of Chemical Physics*, 129(12):121104, 2008.

[20] A. J. Cohen, P. Mori-Sánchez, and W. Yang. Insights into current limitations of density functional theory. *Science*, 321(5889):792–797, 2008.

[21] C. J. Pickard, I. Errea, and M. I. Eremets. Superconducting hydrides under pressure. *Annual Review of Condensed Matter Physics*, 11:57–76, 2020.

[22] T. Yildirim, O. Gülseren, J. W. Lynn, C. M. Brown, T. J. Udovic, Q. Huang, et al. Giant anharmonicity and nonlinear electron-phonon coupling in MgB_2: A combined first-principles calculation and neutron scattering study. *Physical Review Letters*, 87(3):037001, 2001.

[23] M. Calandra and F. Mauri. High-T_c superconductivity in superhard diamondlike BC_5. *Physical Review Letters*, 101(1):016401, 2008.

[24] A. Savin. On degeneracy, near-degeneracy and density functional theory. In *J. M. Seminario (Ed.), Recent Developments and Applications of Modern Density Functional Theory*, pages 327–357. Elsevier, Amsterdam, 1996.

[25] A. D. Becke. Perspective: Fifty years of density-functional theory in chemical physics. *The Journal of Chemical Physics*, 140:18A301, 2014.

[26] V. I. Anisimov, J. Zaanen, and O. K. Andersen. Band theory and Mott insulators: Hubbard U instead of Stoner I. *Physical Review B*, 44(3):943–954, 1991.

[27] J. Zaanen, O. Jepsen, O. Gunnarsson, A. T. Paxton, O. K. Andersen, and A. Svane. What can be learned about high T_c from local density theory? *Physica C*, 153-155:1636–1641, 1988.

[28] J. Zaanen, G. A. Sawatzky, and J. W. Allen. Band gaps and electronic structure of transition-metal compounds. *Physical Review Letters*, 55(4):418–421, 1985. doi: 10.1103/PhysRevLett.55.418.

[29] G. A. Sawatzky and A. Lenselink. Localized vs delocalized description of photoelectron spectra. *The Journal of Chemical Physics*, 72(6):3748–3753, 1980.

[30] O. Gunnarsson and K. Schönhammer. Electron spectroscopies for Ce compounds in the impurity model. *Physical Review B*, 28(8):4315–4339, 1983.

[31] S. Huefner. Photoemission spectra of NiO and CuO. *Solid State Communications*, 49(11):1177, 1984.

[32] I. Pollini, J. Thomas, G. Jezequel, J. C. Lemonnier, and A. Lenselink. Ultraviolet reflectance and electronic states of layered nickel halides studied with synchrotron radiation. *Physical Review B*, 29(8):4716–4726, 1984.

[33] K. Terakura, A. R. Williams, T. Oguchi, and J. Kuebler. Transition-metal monoxides: Band or mott insulators. *Physical Review Letters*, 52(20):1830–1833, 1984.

[34] Y. Ohta, T. Tohyama, and S. Maekawa. Charge-transfer gap and superexchange interaction in insulating cuprates. *Physical Review Letters*, 66(9):1228–1231, 1991.

[35] E. Pavarini, I. Dasgupta, T. Saha-Dasgupta, O. Jepsen, and O. K. Andersen. Band-structure trend in hole-doped cuprates and correlation with $t_{c,\max}$. *Physical Review Letters*, 87(4): 047003, 2001.

[36] H. Sakakibara, H. Usui, K. Kuroki, R. Arita, and H. Aoki. Two-orbital model explains the higher transition temperature of the single-layer Hg-cuprate superconductor compared to that of the La-cuprate superconductor. *Physical Review Letters*, 105(5):057003, 2010.

[37] K.-W. Lee and W. E. Pickett. Infinite-layer $LaNiO_2$: Ni^{1+} is not Cu^{2+}. *Physical Review B*, 70(16):165109, 2004.

[38] Danfeng Li, Kyuho Lee, Bai Yang Wang, Motoki Osada, Samuel Crossley, Hye Ryoung Lee, Yi Cui, Yasuyuki Hikita, and Harold Y. Hwang. Superconductivity in an infinite-layer nickelate. *Nature*, 572(7771):624–627, 2019.

[39] A. S. Botana and M. R. Norman. Similarities and differences between infinite-layer nickelates and cuprates and implications for superconductivity. *Physical Review X*, 10(1):011024, 2020.

[40] N. Metropolis and S. Ulam. The Monte Carlo method. *Journal of the American Statistical Association*, 44(247):335–341, 1949.

[41] W. Krauth. *Statistical Mechanics: Algorithms and Computations*. Oxford University Press, New York, 2006.

[42] N. Metropolis, A. W. Rosenbluth, M. N. Rosenbluth, A. H. Teller, and E. Teller. Equation of state calculations by fast computing machines. *The Journal of Chemical Physics*, 21(6): 1087–1092, 1953.

[43] W. K. Hastings. Monte Carlo sampling methods using Markov chains and their applications. *Biometrika*, 57(1):97–109, 1970.

[44] P. J. Reynolds, D. M. Ceperley, B. J. Alder, and W. A. Lester. Fixed-node quantum Monte Carlo for molecules. *The Journal of Chemical Physics*, 77(11):5593–5603, 1982.

[45] W. M. C. Foulkes, L. Mitas, R. J. Needs, and G. Rajagopal. Quantum Monte Carlo simulations of solids. *Reviews of Modern Physics*, 73(1):33–83, 2001.

[46] A. Szabo and N. S. Ostlund. *Modern quantum chemistry: Introduction to advanced electronic structure theory*. Courier Corporation, 1996.

[47] A. L. Fetter and J. D. Walecka. *Quantum theory of many-particle systems*. Courier Corporation, 2003.

[48] D. J. Thouless. Stability conditions and nuclear rotations in the Hartree-Fock theory. *Nuclear Physics*, 21(2):225–232, 1960.

[49] H. Koch, A. Sánchez de Merás, and T. B. Pedersen. Reduced scaling in electronic structure calculations using Cholesky decompositions. *The Journal of Chemical Physics*, 118(21): 9481–9484, 2003.

[50] E. Y. Loh, J. E. Gubernatis, R. T. Scalettar, S. R. White, D. J. Scalapino, and R. L. Sugar. Sign problem in the numerical simulation of many-electron systems. *Physical Review B*, 41 (13):9301–9307, 1990.

[51] G. Sugiyama and S. E. Koonin. Auxiliary-field Monte Carlo for quantum many-body ground states. *Annals of Physics*, 168(1):1–26, 1986.

[52] S. Zhang, J. Carlson, and J. E. Gubernatis. Constrained-path Monte Carlo method for fermion ground states. *Physical Review B*, 55(11):7464–7473, 1997.

[53] D. M. Ceperley and B. J. Alder. Ground state of the electron gas by a stochastic method. *Physical Review Letters*, 45(7):566–569, 1980.

[54] C. J. Umrigar, M. P. Nightingale, and K. J. Runge. A diffusion Monte Carlo algorithm with very small time-step errors. *The Journal of Chemical Physics*, 99(4):2865–2890, 1993.

[55] H. Shi and S. Zhang. Some recent developments in auxiliary-field quantum Monte Carlo for real materials. *The Journal of Chemical Physics*, 154(2):024107, 2021.

[56] J. Hubbard. Calculation of partition functions. *Physical Review Letters*, 3(2):77–78, 1959.

[57] N. H. F. Beebe and J. Linderberg. Simplifications in the generation and transformation of two-electron integrals in molecular calculations. *International Journal of Quantum Chemistry*, 12(4):683–705, 1977.

[58] M. Burkatzki, C. Filippi, and M. Dolg. Energy-consistent pseudopotentials for quantum Monte Carlo calculations. *The Journal of Chemical Physics*, 126(11):114105, 2007.

[59] W. Purwanto, H. Krakauer, and S. Zhang. Pressure-induced diamond to β-tin transition in bulk silicon: A quantum Monte Carlo study. *Physical Review B*, 80(21):214116, 2009.

[60] W. Ma, W. Purwanto, and S. Zhang. Quantum embedding scheme for the study of localized electronic states in correlated electron systems. *Physical Review B*, 92(23):235109, 2015.

[61] W. Ma, S. Zhang, and H. Krakauer. Auxiliary-field quantum Monte Carlo calculations with plane-wave basis sets. *New Journal of Physics*, 17(2):023016, 2015.

[62] W. Purwanto, S. Zhang, and H. Krakauer. An auxiliary-field quantum Monte Carlo study of the hydrogen molecule dissociation curve. *The Journal of Chemical Physics*, 130(9): 094107, 2009.

[63] R. Balian and E. Brézin. Nonunitary Bogoliubov transformations and extension of Wick's theorem. *Nuovo Cimento B*, 64(1):37–55, 1969.

[64] M. Motta, D. M. Ceperley, G. K. L. Chan, J. A. Gomez, E. Gull, S. Guo, et al. Towards the solution of the many-electron problem in real materials: Equation of state of the hydrogen chain with state-of-the-art many-body methods. *Physical Review X*, 7(3):031059, 2017.

[65] H. Shi and S. Zhang. Symmetry in auxiliary-field quantum Monte Carlo calculations. *Physical Review B*, 88(12):125132, 2013.

[66] James Shee et al. On Achieving High Accuracy in Quantum Chemical Calculations of 3d Transition Metal-Containing Systems: A Comparison of Auxiliary-Field Quantum Monte Carlo with Coupled Cluster, Density Functional Theory, and Experiment for Diatomic Molecules. *Journal of Chemical Theory and Computation*, 15(4):2346–2358, 2019.

[67] A. G. de Oliveira-Filho, F. R. Ornellas, and J. M. Bowman. How to arrive at accurate benchmark values for transition metal compounds: Computation or experiment? *Journal of Chemical Theory and Computation*, 13(11):5291–5306, 2017.

[68] D. Feller, K. A. Peterson, and D. A. Dixon. A survey of factors contributing to accurate theoretical predictions of atomization energies and molecular structures. *The Journal of Chemical Physics*, 129(20):204105, 2008.

[69] N. J. DeYonker, K. A. Peterson, G. Steyl, A. K. Wilson, and T. R. Cundari. Quantitative computational thermochemistry of transition metal species. *The Journal of Physical Chemistry A*, 111(44):11269–11277, 2007.

[70] W. Purwanto, S. Zhang, and H. Krakauer. An auxiliary-field quantum Monte Carlo study of the chromium dimer. *The Journal of Chemical Physics*, 142(6):064302, 2015.

[71] W. Purwanto, S. Zhang, and H. Krakauer. Auxiliary-field quantum Monte Carlo calculations of the molybdenum dimer. *The Journal of Chemical Physics*, 144(24):244306, 2016.

[72] B. O. Roos. The complete active space self-consistent field method. *Advances in Chemical Physics*, 69:399–445, 1987.

[73] G. Carleo and M. Troyer. Solving the quantum many-body problem with artificial neural networks. *Science*, 355(6325):602–606, 2017.

[74] Y.-Y. He, M. Qin, H. Shi, Z.-Y. Lu, and S. Zhang. Finite-temperature auxiliary-field quantum Monte Carlo method: Self-consistent constraint and systematic approach to low temperatures. *Physical Review B*, 99(4):045108, 2019.